Theoretical and Applied Mechanics Letters 14 (2024) 100531

Contents lists available at ScienceDirect

Theoretical and Applied Mechanics Letters

journal homepage: www.elsevier.com/locate/taml

A new cyclic cohesive zone model for fatigue damage analysis of welded vessel

Changyuan Shen [a], Xiaozhou Xia [a,*], Dake Yi [a,*], Zhongmin Xiao [b]

[a] College of mechanical and engineering science, Hohai University, Nanjing 211100, China
[b] School of Mechanical and Aerospace Engineering, Nanyang Technological University, Singapore 999002, Singapore

ARTICLE INFO

Keywords:
Cyclic cohesive zone model
Fatigue crack propagation
Welding residual stress
Low-cycle fatigue
Welded vessel

ABSTRACT

A new cyclic cohesive zone fatigue damage model is proposed to address the fatigue problem spanning high and low cycle stages. The new damage model is integrated with the damage extrapolation technique to improve calculation efficiency. The model's effectiveness in regulating the low-cycle fatigue evolution rate, overall fatigue damage evolution rate, and stress level at the fatigue turning point is assessed through the comparison of the S-N curves. The fatigue damage model's high precision is proved based on the minor deviation of stress at the turning point of the S-N curve from the actual scenario. Finally, the fatigue damage evolution is simulated considering the effects of pre-load pressure and welding residual stress. It is observed that laser welding induces a significant residual tensile stress, accelerating fatigue damage evolution, while compressive loading impedes fatigue damage progression.

1. Introduction. Fatigue is the predominant mode of damage in welded steel structures [1]. Under fatigue loading, cracks form in weldments with defects, involving stages of crack incubation, emergence, propagation, and fracture [2]. In instances of weldments with small weld seams, crack propagation commonly starts from the tip of the weld seam, which can be regarded as the initial crack. Consequently, we can concentrate solely on fatigue crack propagation without considering the crack development process. Pressure vessel weldments frequently experience internal pressure and residual stress, resulting in a complex stress field. This field encompasses a stress amplitude distribution range that extends across the fatigue turning point of S-N curves, necessitating concurrent consideration of high-cycle and low-cycle fatigue. Currently, there is a lack of research that addresses fatigue damage in both weldments and pressure vessels simultaneously. An effective approach is urgently needed to forecast fatigue fracture propagation spanning high and low cycle fatigue in welded vessels.

Currently, conventional approaches to describe fatigue crack propagation mostly rely on the traditional Paris equation. This equation, proposed by Paris et al. in 1963 [3], utilizes an exponential model to illustrate the correlation between the rate of fatigue crack propagation and the stress intensity factor amplitude ΔK:

$$\frac{\mathrm{d}a}{\mathrm{d}N} = C(\Delta K)^m, \tag{1}$$

where a denotes the crack length and N represents the cycles of alternating stress. The parameters C and m are determined by fitting a curve to experimental data [4]. However, the Paris equation is relatively simple and not suitable for complex fatigue issues involving different stress levels or different fatigue stages. Therefore, scholars further refined the Paris equation, creating the Walker model [5] and the Forman model [6] to account for the influence of average stress and the variations in fatigue stages. In the domain of pressure vessels, Shariati et al. conducted fatigue tests on their self-designed thick-walled pressure vessel specimens, and estimated the fatigue crack growth rates by employing a modified Paris model [7]. Importantly, these theories, while offering empirical correlations between the crack propagation rate $\mathrm{d}a/\mathrm{d}N$ and the stress-intensity factor amplitude ΔK, do not explain how fatigue resistance weakens under alternating cycles [8].

The cohesive zone model is commonly used to simulate fatigue crack propagation along predefined paths owing to its unique constitutive established on the traction-separation relationship [9-11]. Different from the Paris equation, the traction-separation relationship in cohesive zone model can account for stiffness loss under external loading [12]. Nguyen et al. [13], Maiti et al. [14] have integrated a material damage evolution model into a linear cohesive model to investigate the fatigue crack propagation process in aluminum alloy panels and polymer materials, respectively. Roe et al. [7] subsequently introduced a cyclic cohesive zone constitutive model that includes an exponential traction separation equation, a fatigue damage evolution equation, and a complex loading and unloading law. Since then, the theory of the cyclic cohesive zone model has matured, and it has been widely adopted to investigate fatigue damage in various types of structures. In recent years, the cyclic

* Corresponding authors.
E-mail addresses: xxz@hhu.edu.cn (X. Xia), 20130037@hhu.edu.cn (D. Yi).

https://doi.org/10.1016/j.taml.2024.100531
Received 22 January 2024; Received in revised form 10 May 2024; Accepted 15 May 2024
Available online 22 May 2024

cohesive zone model has been applied to simulate cracks in pressure-bearing devices or welded parts. For instance, Chen et al. developed a modified cyclic cohesive zone model to predict low-cycle fatigue crack initiation in submarine pipelines. They also proposed an inverse logistic formula to describe the degradation model of cumulative cohesive displacement [15,16]. Wu et al. created a bilinear cohesive model to simulate the tensile process of brazed joints. They studied the impact of cyclic displacement and base material thickness on the fatigue damage process at the interface [17]. However, there has been little focus on concurrent investigations of fatigue failure in welded joints and pressure vessel fatigue issues. Therefore, there is a necessity to establish a new cyclic cohesive zone model to fill this gap.

The study examines the evolution of damage in a pressure vessel with small-sized weld, analyzing the fatigue damage characteristics spanning high and low cycle stages [18-21]. Firstly, based on the conventional cyclic cohesive zone model, a power function term reflecting the curvature of the low cycle S-N curve and a step function term reflecting the stress level at the turning point are introduced. Then, on the ABAQUS software platform, the UMAT module is utilized to secondarily develop the proposed cyclic cohesive fatigue damage constitutive model spanning high and low cycle stages. The residual stress field induced by welding is simulated through the thermal-mechanics coupling module in ABAQUS. This field is imported into the predefined field to explore the fatigue damage mechanism under the action of residual stress.

The structure of this paper is as follows. Section 2 discusses the cohesive fatigue mechanism and develops a new cyclic cohesive zone constitutive model reflecting the fatigue damage behavior across the high and low cycle stages. Section 3 introduces a damage extrapolation strategy aimed at enhancing computational efficiency. The new model's validity is assessed based on the computation results of S-N curves. Section 4 applies the new cyclic cohesive model to simulate the fatigue damage of a welded vessel. Section 5 provides a summary of the relevant conclusions.

2. Improvement of cyclic cohesive zone fatigue damage model.

2.1 Classical cyclic cohesive zone model. The cohesive model, utilized to describe the mechanical behavior of interfaces, is widely employed for simulating and analyzing the initiation and progression of damage in structures with predefined paths. It is frequently combined with fracture and damage methodologies to track the propagation of cracks in metals, ceramics, and composites. Instances include pore nucleation [22], elastic film exfoliation [23], interface fracture [24,25], composite delamination [26,27] and peeling damage [28]. The cohesive model uses the maximum principal stress criterion to identify the point when damage starts and stiffness decreases, while the power law fracture criterion is employed to indicate material failure. These two criteria serve to establish the effective displacement at the start of damage and fracture failure [29], respectively. Combined with the maximum effective displacement $\delta_{\max}$ in the current loading process, the damage D_{m} resulting from static loading is defined as:

$$D_{\mathrm{m}} = \frac{\delta_{\mathrm{n}}^{\mathrm{f}}\left(\delta_{\max} - \delta_{\mathrm{n}}\right)}{\delta_{\max}\left(\delta_{\mathrm{n}}^{\mathrm{f}} - \delta_{\mathrm{n}}\right)}, \tag{2}$$

where δ_{n} is the displacement of damage initiation, and $\delta_{\mathrm{n}}^{\mathrm{f}}$ represents the displacement when interface failure occurs.

The constitutive relation in the cohesive model [30] is illustrated in Fig. 1. When the current maximum displacement is less than δ_{n}, no damage occurs, and the stress-strain relationship is linear, as shown in the ascending portion of Fig. 1. When $\delta_{\max}$ exceeds δ_{n}, according to Eq. (2), the stiffness E of the material begins to degenerate, leading to the emergence of damage that progressively intensifies. Once $\delta_{\max}$ reaches $\delta_{\mathrm{n}}^{\mathrm{f}}$, the damage value reaches 1, and the interfacial traction is completely released, as shown in the descending section of Fig. 1.

In the fatigue failure process, the constitutive model of the cyclic cohesive element has been enhanced in two aspects: the modification of the damage evolution equation and the addition of a loading and unloading law. The damage evolution equation now incorporates the

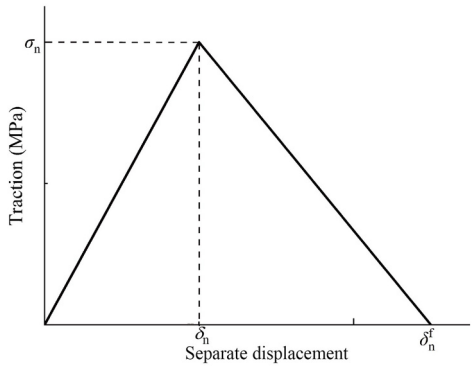

Fig. 1. Constitutive relationship curve of the cohesive model.

combined effect of alternating and static loads. In this equation, the fatigue damage increment, denoted as $\dot{D}_{\mathrm{f},}$ is expressed as follows:

$$\dot{D}_{\mathrm{f}} = \frac{\Delta\dot{\bar{u}}}{\delta_{\Sigma}}\left(\frac{T}{\sigma_{\mathrm{res}}} - C_{\mathrm{f}}\right)H\left(\Delta\bar{u} - \delta_0\right), \tag{3}$$

where $\Delta\bar{u}$ represents the cumulative tension displacement under alternating load, the tensile displacement generated in each incremental step accumulates in $\Delta\bar{u}$; δ_0 represents the characteristic tensile displacement; and H denotes the Heaviside function, whose value takes 1 or 0 respectively when the independent variable is positive or negative. The presence of $H(\Delta\bar{u} - \delta_0)$ in Eq. (3) indicates that cumulative displacement $\Delta\bar{u}$ becomes effective only when it surpasses the characteristic tensile displacement δ_0, leading to cumulative fatigue damage. Moreover, δ_{Σ} denotes the cumulative cohesive displacement, and is used to scale the normalized increment of the effective material separation. This parameter governs the accumulation of effective tensile displacement for interfacial failure, ensuring that the fatigue damage D_{f} remains within the range of 0 to 1. Specifically, δ_{Σ} equals $\Delta\bar{u}$ when fatigue damage D_{f} reaches 1. The magnitude of δ_{Σ} is an integer multiple [8] of δ_0, with the actual multiple values increasing as the fatigue resistance of materials improves. Here, T represents the traction force at the interface, σ_{res} signifies the current residual strength of the material. It is expressed as the product of the initial strength σ_{n} and undamaged weight (1-D). C_{f} denotes the minimum stress amplitude ratio necessary for fatigue damage initiation, serving as the threshold.

The static damage remains consistent with the conventional cohesive model in Eq. (2), so the static damage increment $\dot{D}_{\mathrm{m}}$ is expressed as follows:

$$\dot{D}_{\mathrm{m}} = D_{\mathrm{m}|t} - D_{\mathrm{m}|t-\Delta t}. \tag{4}$$

Having defined two different damage mechanisms, the larger of the two values is always stored as the current damage increment:

$$D = \int \max\left(\dot{D}_{\mathrm{m}},\ \dot{D}_{\mathrm{f}}\right)\mathrm{d}t. \tag{5}$$

Combining Eq. (4) with Eq. (2), the static damage D_{m} at the beginning and end of each incremental step can be calculated, and then the static damage increment $\dot{D}_{\mathrm{m}}$ can be obtained. During alternating stress loading, both fatigue damage D_{f} and static damage D_{m} occur simultaneously, the larger one will prevail. This mechanism can be attributed to the classic cyclic cohesion model proposed by Roe [8].

The current material stiffness E, residual strength σ_{res}, and stress amplitude ratio C_{f} in the damage evolution model are given by the following equations:

$$E = (1 - D)E_0, \tag{6}$$

$$\sigma_{\mathrm{res}} = (1 - D)\sigma_{\mathrm{n}}, \tag{7}$$

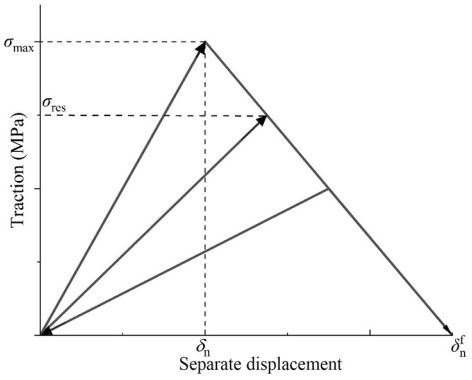

Fig. 2. Loading-unloading law for the cyclic cohesive model.

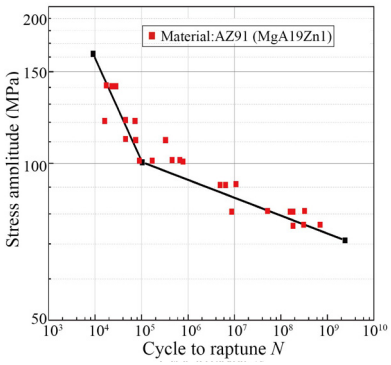

Fig. 3. Double logarithmic S-N curve with turning point.

$$C_f = \frac{\sigma_f}{\sigma_n},\ 0 < C_f < 1, \tag{8}$$

where E_0 represents the initial stiffness, σ_n represents the initial strength of the material, and σ_f is the lower limit of stress amplitude at which fatigue damage begins.

Figure 2 illustrates the loading and unloading law of the fatigue cohesive model, indicating that when alternating stress exceeds a certain threshold, the current residual material strength σ_{res} decreases with each successive cycle, and the effective displacement σ_n at the onset of damage increases. It is important to note that the curve shown in Fig. 2 applies only to cases where D_m is greater than D_f. For cases where fatigue damage predominates, please refer to Fig. 19, in which the damage evolution is nonlinear.

2.2 The cyclic cohesive fatigue damage model spanning high and low cycle stages. Conventional cohesive models do not distinguish the fatigue mechanisms between high and low cycle stages, maintaining a uniform structure. However, in reality, the S-N curves of certain metallic materials exhibit turning points from high to low cycle fatigue [18], as shown in Fig. 3. The figure illustrates the double logarithmic S-N curve of MgAl9Zn1, a commonly utilized material in the manufacturing industry. At about 100,000 cycles, a transition point is observed, as shown in Fig. 3. This indicates a shift in fatigue mode from high to low cycle, which needs to be incorporated into the new model.

The construction of the new model necessitates the development of new built-in parameters. The existing parameters of the model include T, $\Delta\bar{u}$, δ_Σ, C_f, δ_0, and σ_n as indicated from Eq. (3) to Eq. (8). Obviously, the new fatigue mechanisms must be achieved by altering the material's strength property σ_n, independent of the external load T, thresholds C_f and δ_0, or the state variable $\Delta\bar{u}$. Thus, propagation parameters α and β are introduced into the term σ_n to reflect new fatigue mechanisms. The critical parameter α regulates the stress level at the onset of low-cycle fatigue, while the evolution parameter β controls the damage acceleration, manifested by the slope of the S-N curve in the low-cycle fatigue stage.

The modified evolution equation for fatigue damage is expressed as follows:

$$\dot{D} = \frac{\Delta\dot{\bar{u}}}{\delta_\Sigma}\left[\frac{T}{\sigma_{res} - \exp\left(\frac{-\beta\sigma_{res}}{T-\alpha\sigma_{res}}\right)\sigma_{res}H\left(T-\alpha\sigma_{res}\right)} - C_f\right]H\left(\Delta\bar{u}-\delta_0\right),\ D \le 1. \tag{9}$$

The stress turning point σ_t is defined as follows:

$$\sigma_t = \alpha\sigma_{res}, \tag{10}$$

where σ_t is directly obtained from the S-N curve, σ_{res} takes the value of static strength σ_n when the material is undamaged. Thus, α can be obtained as the ratio of σ_t and σ_n.

The basis for modifying the model will be elucidated as follows. We observe that Eq. (3) consists of three components: $\Delta\dot{\bar{u}}/\delta_\Sigma$, $(T/\sigma_{res} - C_f)$, $H(\Delta\bar{u} - \delta_0)$. The first component $\Delta\dot{\bar{u}}/\delta_\Sigma$ controls the overall damage evolution rate, while the third component $H(\Delta\bar{u} - \delta_0)$ and parameter C_f determine the threshold of fatigue damage, both of which are independent of model improvement.

The modified model is required to maintain consistency with the conventional model in the high-cycle stage while reflecting the new fatigue characteristics in the low-cycle stage, thus necessitating the introduction of $H(T - \alpha\sigma_{res})$ into the second component. When $T \le \alpha\sigma_{res}$, the function $H(T - \alpha\sigma_{res})$ takes the value of 0, thereby reducing Eq. (9) to the conventional model, as depicted in Eq. (3). When $T \ge \alpha\sigma_{res}$, The model transitions into the low cycle stage.

The new model in the low-cycle stage must satisfy the following conditions:

(1) Continuity of the function must be ensured, meaning: $\lim_{T\to(\alpha\sigma_{res})^+}\dot{D} = \lim_{T\to(\alpha\sigma_{res})^-}\dot{D}$.
(2) It is essential to ensure immediate fracture under the limiting condition when T reaches the strength σ_n and β tends to 0, which implies: $\lim_{\substack{T\to\sigma_{res}\\ \beta\to 0}}\dot{D} \ge 1$.
(3) As β decreases, the damage increment $\dot{D}$ will increase to reflect different rates of damage acceleration.

To meet these three requirements, a power function $\exp(-\beta\sigma_{res}/T - \alpha\sigma_{res})$ is introduced. When the external load T tends to $(\alpha\sigma_{res})^+$, the power function $\exp(-\beta\sigma_{res}/T - \alpha\sigma_{res})$ tends to 0, and when T tends to $(\alpha\sigma_{res})^-$, $H(T - \alpha\sigma_{res})$ approaches 0, thus satisfying condition (1). When $T = \sigma_{res}$, the damage increment $\dot{D}$ reaches its maximum value $\Delta\dot{\bar{u}}/\delta_\Sigma \cdot \{T/[\sigma_{res} - \sigma_{res}\exp(-\beta/1-\alpha)] - C_f\}$, and at this point, $\dot{D}$ tends to infinity if β tends to 0, indicating the transformation of fatigue failure into unstable failure. Finally, the third condition is naturally satisfied because of the introduction of a negative exponential power function. Overall, the power function and step function with two new parameters effectively fulfill the three requirements, making the new model theoretically effective.

A segment of the Fortran subroutine for the new cyclic cohesive model, along with the corresponding flow chart, is provided in Figs. 4 and 5. According to the different stress and displacement at the cohesive interface, three kinds of damage calculation formulas are assigned.

3. Damage extrapolation and model validation.

3.1 Effectiveness validation of the damage extrapolation technique. In medium and high cycle fatigue, each loading induces slight damage. Utilizing conventional direct cycle techniques, such as the direct cycle analysis step in ABAQUS, would require 10^4 to 10^7 cycles for damage value D to approach 1, resulting in time-consuming calculations. More inconveniently, it is difficult to combine the direct cycle analysis step with the cyclic cohesive model to simulate the S-N curve with a turning point. Therefore, a method that can be built into the cyclic cohesive

```
IF(DELTT.GT.DELTA_O.AND.D_OLD.LT.ONE)THEN  ! Calculate the damage increment above the
                                           cumulative displacement threshold
  IF(TEMP4.GE.TEMP5)THEN                   ! Damage growth during interface opening
    IF(TEMP6.GE.(Alpha*SIGMA_M))THEN       ! The situation after entering low cycle fatigue
    DC = ABS(TEMP4-TEMP5)/(3*DELTA_O)* (TEMP6/(SIGMA_M-TEMP6*DEXP(-Beta*
    SIGMA_M/(0.01+TEMP6-Alpha*SIGMA_M)))-CF)
                                           ! New cyclic cohesion model
    DC = MAX(ZERO,DC)
    DC = MIN(ONE,DC)
    STATEV(7) = 1
    CP = STATEV(7)                         ! Low cycle fatigue state was recorded
    ELSE
    DC = ABS(TEMP4-TEMP5)/(3*DELTA_O)*(TEMP6/SIGMA_M-CF)
                                           !Traditional cyclic cohesion model
    DC = MAX(ZERO,DC)
    STATEV(7) = 0                          ! The middle-high cycle fatigue state was recorded
    ENDIF
  ELSE
     DC=ZERO
  ENDIF
ELSE
    DC = ZERO
```

Fig. 4. Partial Fortran subroutine for the new cyclic cohesive zone model.

model to accelerate the damage accumulation rate and reduce the number of cycles is needed, which is called damage extrapolation technology.

Assuming the finite element simulation needs to simulate a total of N cycles, and the cumulative cohesive displacement denoted as δ_Σ is multiplied by a function $f(k)$ related to the extrapolation factor k, resulting in the new cumulative cohesive displacement $\delta_\Sigma f(k)$. According to the concept of the damage extrapolation technique, loading $N/f(k)$ times suffice to obtain the final result. This method is mainly to amplify a certain number of times of a parameter to accelerate the fatigue damage accumulation rate, so that the result of simulating a cycle loading is equal to the result of loading $f(k)$ times in reality. In this study, we set $f(k) = k$ and employed a flat plate with a cyclic cohesive zone weld interface to assess the accuracy of this method. As shown in Fig. 6, an alternating load is applied to both surfaces of the flat plate, the fatigue damage constitutive model proposed in this paper is given to the middle weld interface by using the user subroutine UMAT in ABAQUS, and then the calculation of damage accumulation is carried out.

During the validation of the damage extrapolation technique, we set k to 1, 10, and 50, respectively, and conducted 2800, 280, and 56 cyclic loading based on these magnification factors. This corresponds to simulating 2800 times with the parameter δ_Σ. If the results obtained are substantially similar, it affirms the feasibility of the damage extrapolation technique. When the difference surpasses the accuracy of fatigue

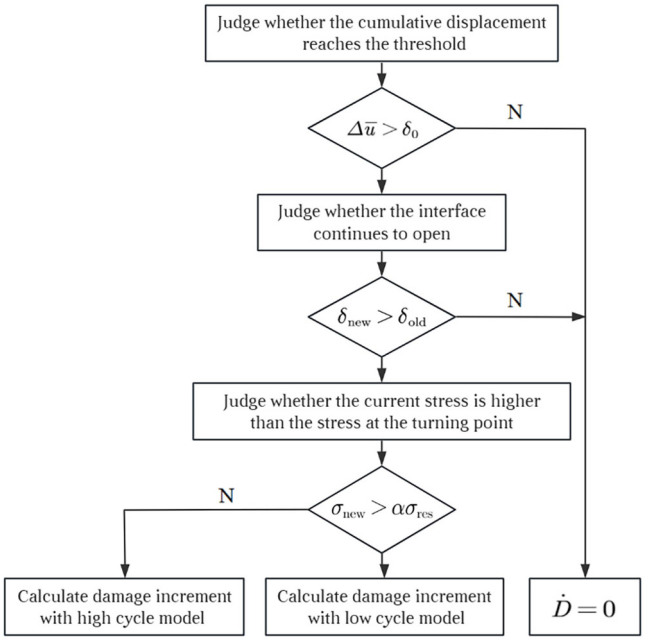

Fig. 5. Flow chart of new cyclic cohesive model.

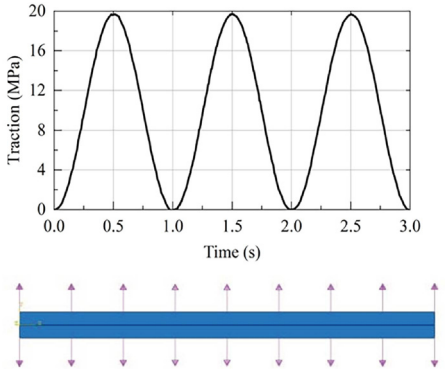

Fig. 6. The alternating load curve on the flat plate.

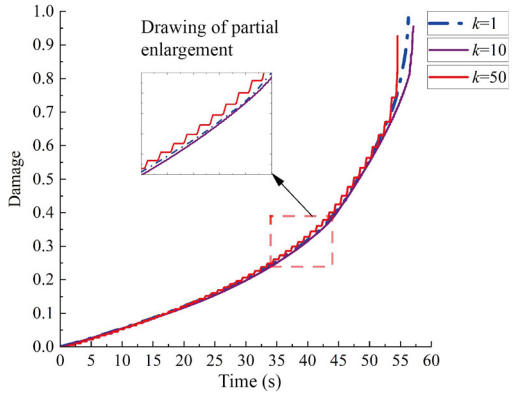

Fig. 7. Damage evolution curves for different extrapolation factors.

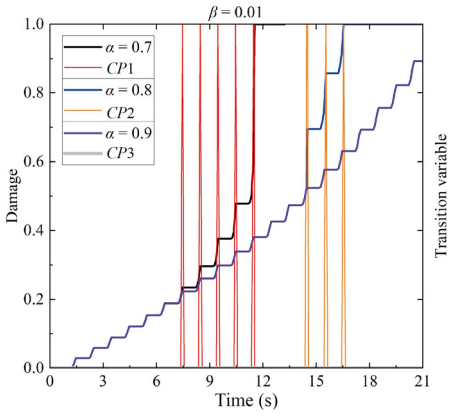

Fig. 8. Damage evolution curves with different critical factor α ($\beta = 0.01$).

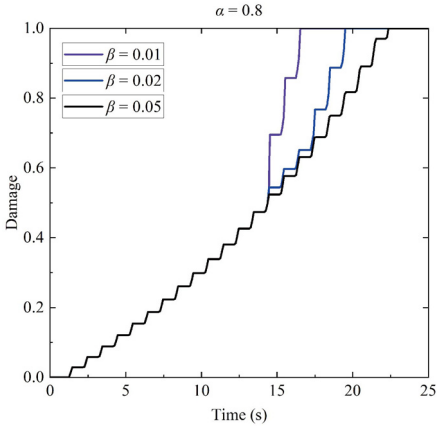

Fig. 9. Damage evolution curves with different evolution parameter β ($\alpha = 0.8$).

prediction, it suggests that the damage extrapolation technique is not feasible. In this calculation, parameters α, β, and δ_Σ take the values of 0.7, 0.02, and $5\delta_0$ respectively. It is worth noting that in the damage extrapolation case and the welded vessel case in Section 4, the value of δ_Σ is small ($\delta_\Sigma = 250\delta_0$), while in the simulation of the S-N curve, the value of δ_Σ is more realistic ($\delta_\Sigma = 100,000\delta_0$). This difference arises because the damage extrapolation and welded vessel cases belong to qualitative analysis in this study, where a simplified calculation with a variable-controlling approach is adopted. A larger amount of calculation is allocated to the quantitative analysis of the S-N curve to verify the fatigue characteristics of the model.

A comparison of the damage evolution at three different magnification factors is depicted in Fig. 7. The damage evolution trends obtained under these factors consistently show a rapid increase from 0 to 1. The local enlargement figure shows that while the incremental stages for the three amplification factors varied, the damage evolution results are essentially the same across the entire stage. In conclusion, increasing the extrapolation factor in damage extrapolation technology has minimal impact on damage evolution outcomes. The results of the calculations show that it is possible to use damage extrapolation technology to efficiently replicate high-cycle fatigue damage with fewer cycles. Finally, the appropriate damage extrapolation factor k is determined to be 50 and will be applied to the calculation of the S-N curve.

3.2 Effectiveness validation of the propagation parameters. Propagation parameters α and β, along with the cohesive displacement δ_Σ, directly influence the accumulation rate of the damage increment, which in turn influences the lifespan of the welding interface and the shape of the S-N curves. Therefore, damage evolution curves and logarithmic S-N curves are employed to validate the effectiveness of these parameters.

A brief qualitative analysis of the propagation parameters is performed using damage evolution curves. Smaller values of δ_Σ were chosen to enhance observation and save computational resources, which increased the rate of damage accumulation. To monitor the influence of the propagation parameters on the crack propagation rate, two state variables—fatigue damage value D and the high and low cycle transition variable CP—were defined in the user subroutine UMAT. In the low-cycle fatigue stage ($T \geq \alpha\sigma_{\text{res}}$), CP is set to 1, while in the high-cycle fatigue stage, it is set to 0.

Figure 8 illustrates the fatigue damage D at the weld interface and the fatigue transition variable CP. In this case, α is set to 0.7, 0.8, and 0.9, while β is 0.01. If α is 0.9, no low-cycle fatigue occurs, and the value of $CP3$ consistently stays at 0. In this scenario, the development curve of $CP3$ aligns with the horizontal axis and is not displayed in the figure.

As shown in Fig. 8, the time point where the transition variable reaches 1 aligns with the initiation point of low-cycle fatigue and a smaller α leads to an earlier onset of low-cycle fatigue. When α is increased to 0.9, the stress value at the weld tip is insufficient to reach the stress value at the fatigue turning point, consequently, the damage evolution curve remains entirely in the high-cycle fatigue stage. Specifically, when α is set to 0.7 and 0.8, the damage evolution curves enter the low-cycle evolution stage at 7.45 s and 14.45 s, respectively. Before these points, the evolution curves are identical, representing the same high cycle fatigue damage evolution process.

Figure 9 displays fatigue damage evolution curves for different values of β (0.01, 0.02, and 0.05) while maintaining α at a constant value of 0.8. Additionally, Fig. 10 compares the transition variable for different values of β. It is evident that a smaller evolution parameter β leads to a faster damage evolution rate in the low-cycle fatigue stage. Importantly, the size of β does not impact the starting point of low-cycle fatigue, which is controlled solely by α.

The above simulations aimed to compare the fatigue crack propagation process by altering the values of the propagation parameters α and β. Recorded fatigue damage development at the weld interface shows that adjusting critical parameter α and evolution parameter β values can result in variable fatigue turning points and low-cycle evolution rates.

Subsequently, the validity of the propagation parameters α and β is confirmed by comparing S-N curves. The critical parameter α is fixed at 0.4, the initial strength of the material σ_n is 300 MPa, and the evolution parameters β are set to 0.03, 0.05, and 0.08, respectively. With other parameters unchanged, the finite element calculation is conducted to determine the life of the interface when fatigue failure occurs (when $D = 1$) under different amplitudes of external loads, and the S-N curve shown in Fig. 11 is made.

As the critical parameter α remains constant, the three curves overlap below the turning point in Fig. 11. The stress at the simulated turning point is 125 MPa, which is defined by the stress value at the intersection of three S-N curves. The theoretic turning point stress defined as $\alpha\sigma_n$

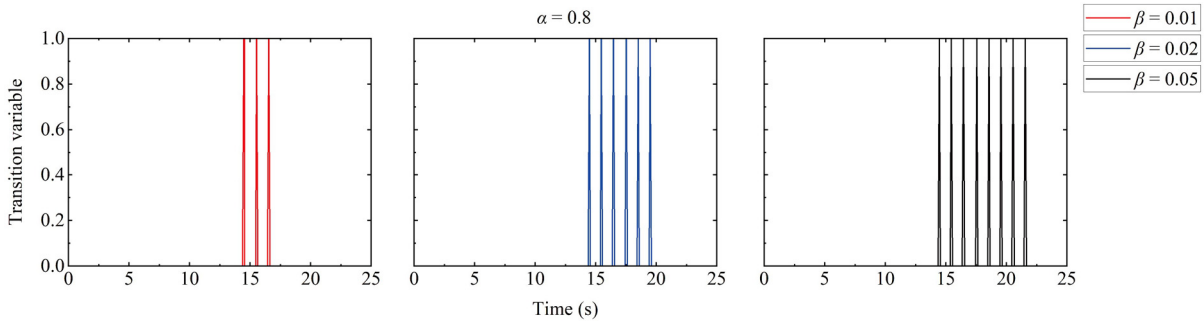

Fig. 10. Transition variable curves with different evolution parameter β.

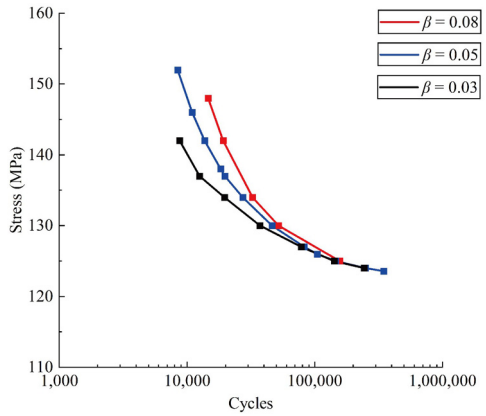

Fig. 11. S-N curves with different evolution parameter β.

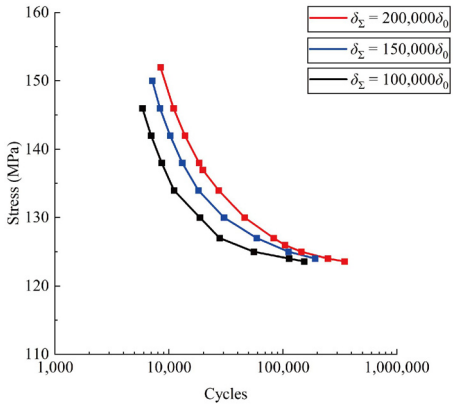

Fig. 13. S-N curves with different cohesive displacement δ_Σ.

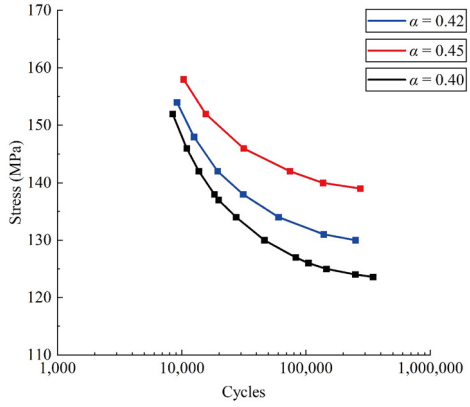

Fig. 12. S-N curves with different critical parameter α.

is taken as 120 MPa which is slightly lower than the simulated turning point. This discrepancy is attributed to the slow initial growth rate of the exponential model above the turning point, requiring a slight increase in stress to reflect the difference in damage evolution. Above the simulated turning point, the three curves exhibit an accelerated evolutionary trend at varying rates due to differences in the evolution parameter β.

Next, the evolution parameter β is fixed at 0.05, and the critical parameter α is set to 0.4, 0.42, and 0.45, respectively, with other parameters unchanged for the calculation. The resulting S-N curves are presented in Fig. 12. Due to the consistent propagation parameters, the three curves follow a similar trend. The curves with larger critical parameters are relatively shifted upward. According to the initial stress of 300 MPa and the value of α taken in Fig 12, the theoretic turning points for the three curves are 120 MPa, 126 MPa, and 135 MPa, while the corresponding simulated turning points are 125 MPa, 131 MPa, and 140 MPa, respectively. The result is in an error of approximately 3.6%–4.2%, which aligns with the accuracy requirements.

Finally, the cumulative cohesive displacement δ_Σ is observed on the S-N curve. According to the damage evolution equation, δ_Σ controls the overall rate of damage evolution and constrains the fatigue life at different stress amplitudes, irrespective of the cycle stages. These three curves in Fig. 13 correspond to cases that δ_Σ take 200,000δ_0, 150,000δ_0, and 100,000δ_0. Due to the consistent propagation parameters α and β, these three curves exhibit similar developmental trends. The value of δ_0 decreases as the curve moves to the left, indicating a faster overall process of fatigue failure.

These simulations show that the propagation parameters α and β play a significant role in controlling the stress magnitude at the turning point and the curvature of the S-N curve during the low-cycle fatigue stage. Besides, the cumulative cohesive displacement δ_Σ controls the overall damage evolution rate, facilitating the horizontal movement of the S-N curve.

In this section, the damage evolution trend of the cyclic cohesive zone element and the distribution of the S-N curves for various parameter values are compared through numerical simulations. By adjusting the inherent parameters of the new cyclic cohesive zone model, it is possible to effectively match S-N curves with various material fatigue characteristics, the effectiveness of the propagation parameters is thus confirmed.

4. Fatigue damage simulation of welded vessels. The longitudinal axisymmetric section of the studied welded vessel is presented in Fig. 14(a). The annular configuration results in a centrosymmetric post-weld residual stress field. Consequently, the geometric model can be simplified into a two-dimensional axisymmetric form. Inside the vessel, there is a pressure sensor device in the pressurized part, which is supported externally by a base. The fusion pool and unfused welding seam meet at their junction. The Extended Finite Element Method [31] is ap-

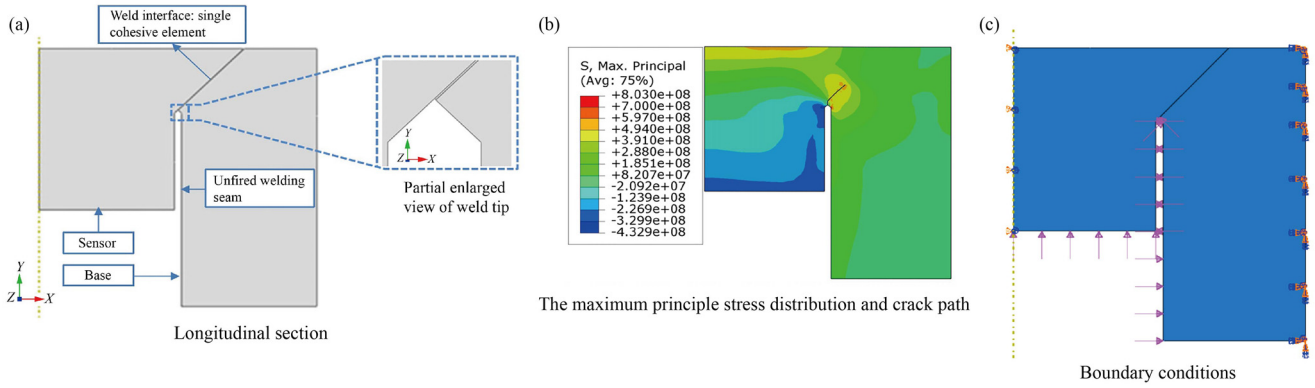

Fig. 14. Welded vessel model.

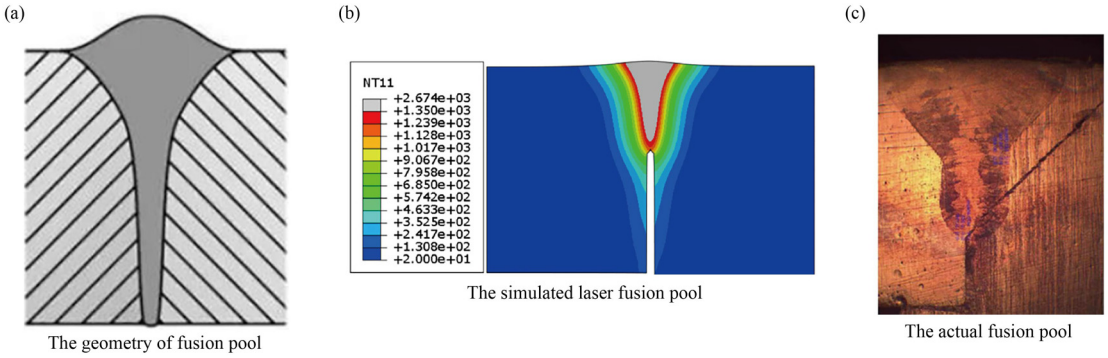

Fig. 15. Comparison of laser welding pool.

Table 1
Material parameters of pressure vessel.

	Thermal conductivity ($W\cdot(m\cdot K)^{-1}$)	Coefficient of thermal expansion (K^{-1})	Specific heat capacity ($J\cdot(kg\cdot°C)^{-1}$)	Modulus of elasticity (Pa)	Poisson's ratio	Intensity ($kg\cdot m^{-3}$)
20 °C	15.11	1.73×10^{-5}	502	1.95×10^{11}	0.3	7890
1000 °C	23.1	1.90×10^{-5}	502	1.50×10^{11}	0.3	7890

plied to simulate the path of crack propagation and verify the location of the cohesive interface.

The model's length and width are both 20 mm. Symmetric boundary conditions are applied to the model's symmetry axis, and fixed boundary conditions are implemented at the outer face to simulate the clamping and fixing process of welding. Uniform pressure is distributed on the inner surface of the model. The boundary condition is depicted in Fig. 14(c). The maximum principal stress damage criterion is selected with the stress set to 400 MPa, the damage evolution criterion is bilinear, and the fracture energy is set to 42,200 J/m^2. The simulation result, presented in Fig. 14(b), indicates that the crack paths extend at a 45° angle to the longitudinal direction. Thus, the location of the cohesive interface can be determined, as shown in Fig. 14(a). The crack position aligns with the experimental result, and the crack path under the pressure test can be referenced in Fig. 15(c). The experiment shows that cracks at around a 45° angle form around the fusion pool under different pressure settings.

Subsequently, fatigue failure simulation of the weld interface is carried out, involving two distinct steps: coupled thermal-mechanical analysis of the weld residual stress field and the damage calculation of the fatigue interface under the residual stress field.

316 L steel was selected for transient coupled temperature-displacement analysis, with particular material parameters listed in Table 1 for both thermal and mechanical categories. A composite heat source DFLUX subroutine was designed in ABAQUS to replicate the laser welding heat source, overcoming the default limitation of only allowing either a surface heat source or a body heat source independently. To accurately replicate the structure of the fusion pool, a composite heat source was selected, comprising a double ellipsoidal body heat source and a Gauss surface heat source, as the heat input. A comparison between the simulated fusion pool and the actual fusion pool is shown in Fig. 15(b) and (c). Notably, the geometric shape is wider above and narrower below, which is a typical feature of a laser fusion pool.

Since the workpiece experiences a multi-axial stress state, relying solely on a single principal stress is inadequate for capturing the tensile and compressive states within the material. To address this, the maximum principal stress, the absolute value of the larger principal stress, and the hydrostatic pressure were chosen for observation. These three quantities were recorded in ABAQUS as "max principal stress", "max principal (abs) stress", and "pressure", where "pressure" represents the opposite number of the average of the three principal stress.

The distribution of the maximum principal stress at the initiation of welding is illustrated in Fig. 16. Along the symmetric path at both ends of the heat source, the thermal stress distribution is depicted in Fig. 17. Near the center of the heat source, there is a substantial tensile stress, gradually diminishing to zero with increasing distance from the center. Compressive stress is noticeable in the core of the heat source. The phenomenon occurs as a result of thermal expansion caused by the

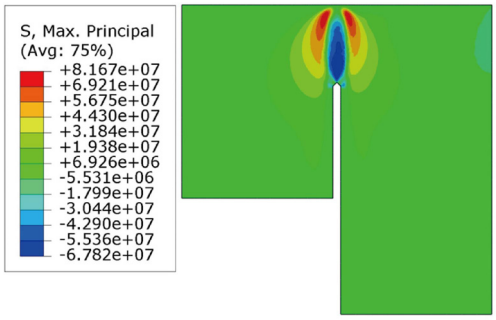

Fig. 16. The stress distribution at welding initiation (Pa).

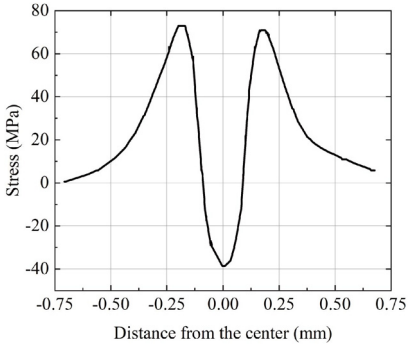

Fig. 17. The stress distribution along the symmetric path (MPa).

high energy concentration in laser welding, which is constrained by the surrounding materials, leading to significant compressive stress.

Subsequently, the distribution of max principal (abs) stress and pressure throughout the entire process, from the initiation of welding to the end of cooling, is observed. The entire simulation comprises a heating analysis step of 0.5 s and a cooling analysis step of 900 s, with special attention given to the transition between the two steps. The calculation results are presented in Fig. 18(a) and (b). The corresponding times of the three pictures are 0.5 s, 0.501 s, and 0.51 s respectively, representing the stress distribution at the end of welding, at the beginning of cooling, and during cooling, from left to right. Near the welding heat source, the tensile stress in the three images exhibits a rapidly increasing trend.

The analysis reveals that the material at the center of the heat source experiences compressive stress during the welding process due to nonlinear heat input. During the cooling process, significant residual compressive plastic deformation persists in the center of the heat source, which does not return to its original dimensions. Conversely, the material around the heat source recovers more rapidly; as a result, the center of the heat source undergoes tensile stress imposed by the surrounding material, leading to residual tensile stress in the weld.

Next, fatigue damage calculations are performed within the residual stress field. The vessel is subjected to a cyclic pulsating load to replicate an alternating pressure environment, based on the fatigue load-time curve shown in Fig. 6. The cyclic cohesive zone model established with the UMAT subroutine is then applied to the cohesive element located at the weld interface. At the beginning of each incremental step, ABAQUS transfers the stress, damage, and strain increments to the subroutine as initial values. The UMAT subroutine calculates the stiffness matrix and derives stress state and damage values at the end of each incremental step. This approach enables real-time tracking of damage evolution. The material properties mentioned are the same as those listed in Table 1 from the preceding section.

The stress-strain curve of the material at the weld tip is obtained upon completing the calculation and is illustrated in Fig. 19. During the first cycle under fatigue loading, the stress-strain curve exhibits a linear relationship, with the slope indicating the initial stiffness of the material. As the number of cycles increases, the material strength gradually decreases. In each cycle of the alternating load, the maximum displacement at the interface increases, while the maximum stress decreases. The stress-strain curve is nonlinear and irreversible in the rising stage, while in the interface closing stage, the stress is unloaded linearly because no damage accumulates.

Subsequently, the influence of welding residual stress on the fatigue crack propagation rate is examined. The residual stress field determined at 700 W power is integrated into the fatigue model as a predefined field. The pressure vessel is subjected to a 60 MPa pressure, and the damage evolution of the weld tip element is monitored during the calculation. The results are contrasted with those under the non-residual stress condition, and the comparative outcomes are shown in Fig. 20.

Figure 20 clearly shows that fatigue damage progresses more rapidly in the post-welding state, with the residual tensile stress playing a crucial role in promoting fatigue damage development.

Considering that welding residual tensile stress can accelerate the development of fatigue damage, an analysis was conducted to determine whether the pre-load compressive stress can hinder fatigue crack propagation. A cohesive model was adopted with parameters $\alpha = 0.8$ and $\beta = 0.05$, and an additional 100 MPa compressive stress is applied to the pressure vessel's surface. The comparison of fatigue damage evolution results is illustrated in Fig. 21, where Fig. 21(a) depicts the damage evolution at the end of the weld (i.e., the front end of the crack), and Fig. 21(b) displays the damage evolution at the back end of the crack interface.

The comparison reveals that pre-load compressive stress has little impact on damage evolution at the tip of the weld, primarily due to the obvious stress concentration phenomenon in that area. However, the pre-load stress effectively inhibits damage evolution at the end of the path. This observation indicates that while the compressive stress may have limited effect in delaying the initiation time point of the crack, it demonstrates efficacy in slowing down the overall crack propagation process.

5. Conclusion. This study explores the fatigue characteristics of pressure vessels with small welded seams, focusing on the progression of fatigue damage spanning high and low cycle stages. A new cyclic cohesive zone fatigue damage model is proposed, encompassing two stages of fatigue crack propagation. The model accounts for the reduction in material stiffness in the high-cycle fatigue damage stage and manages the development of low-cycle fatigue damage. An accelerated simulation method known as the damage extrapolation methodology is used to simulate millions of cycles. This method greatly improves the computational efficiency of the fatigue damage evolution process, speeding up the evaluation of fatigue life for welded vessels. Some conclusions are summarized as follows:

(1) The newly proposed cyclic cohesive zone model allows for separate manipulation of the stress level at the turning point from high to low cycle fatigue by adjusting the critical parameter α. The evolution parameter β effectively regulates the damage evolution rate of low-cycle fatigue, while the cumulative cohesive displacement δ_Σ controls the overall evolution rate. The simulated turning point deviates by 3.6%–4.2% from the theoretical turning point, which is within the acceptable range of less than 5%, confirming the efficacy of the proposed model.

(2) The outcomes of the fatigue damage simulation for welded pressure vessels using the developed cyclic cohesive zone model indicate a reduction in material stiffness during the alternating cycle. Each cycle results in an increase in the maximum separation displacement and a drop in the maximum stress at the crack ends, which aligns with real-world measurements.

(3) Thermal coupling simulations show that intense compressive stress forms close to the heat source during welding, attributed to ther-

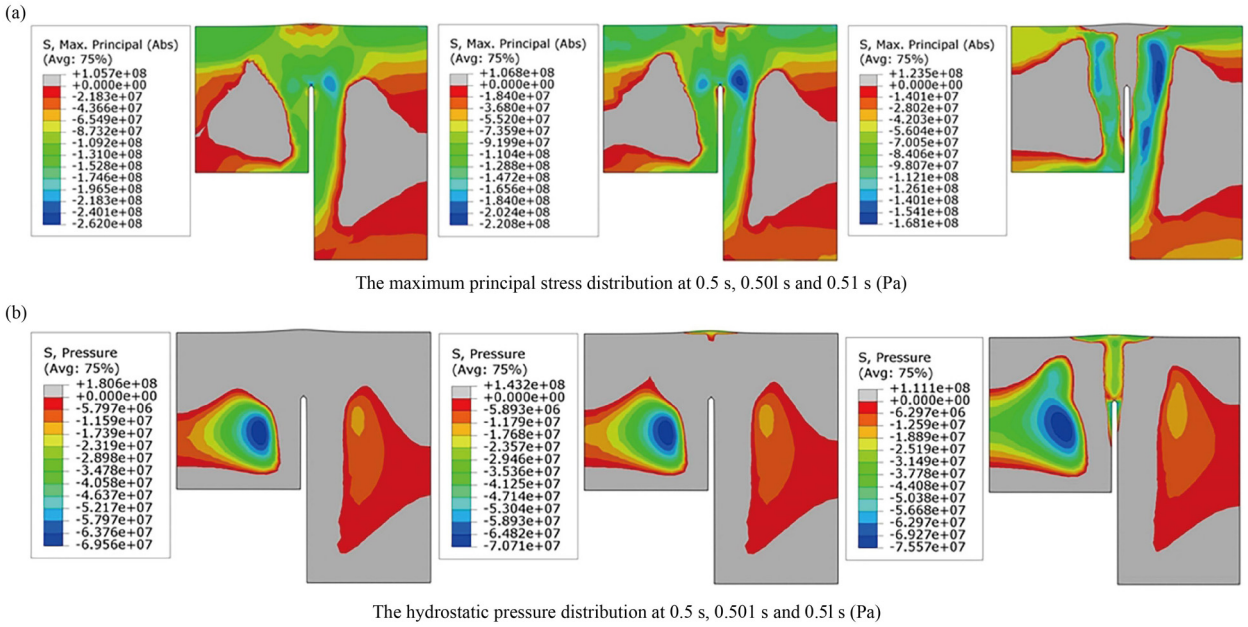

Fig. 18. Comparison of stress distribution at the end of welding.

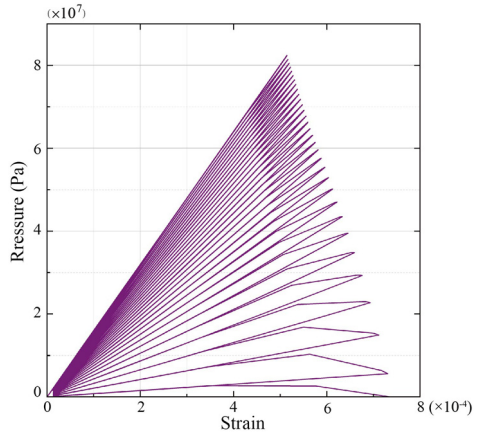

Fig. 19. The stress-strain curves at the weld tip.

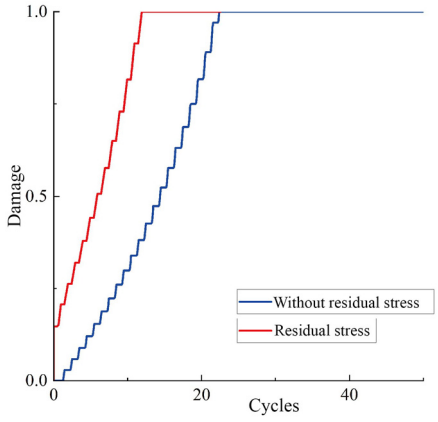

Fig. 20. Comparison of fatigue damage evolution before and after welding.

mal expansion effects. Subsequently, during the post-weld cooling state, material deformation around the heat source recovers rapidly, resulting in significant residual tensile stress in the central region where large plastic deformation persists.

(4) Residual tensile stress significantly speeds up the damage evolution process in the post-weld situation. Pre-load compressive stress on the pressure vessel surface does not significantly postpone the crack initiation time but retards the damage evolution and crack propagation rate.

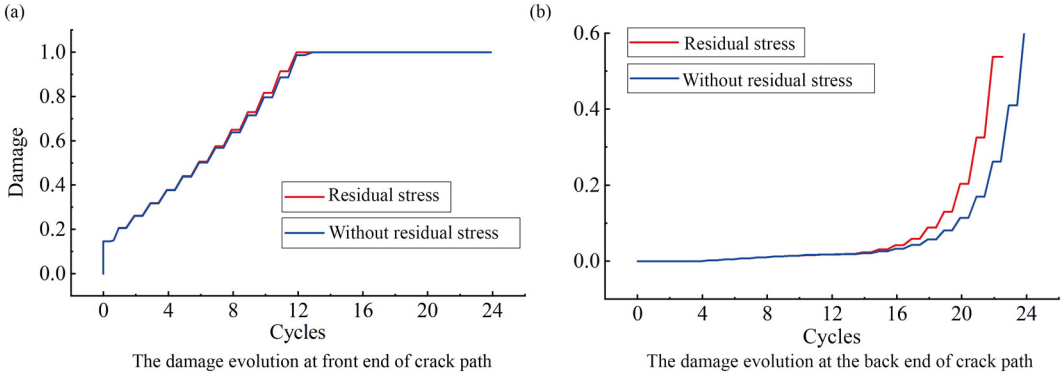

Fig. 21. Comparison of fatigue damage evolution before and after welding.

Declaration of competing interest

The authors declare that they have no known competing financial interests or personal relationships that could have appeared to influence the work reported in this paper.

CRediT authorship contribution statement

Changyuan Shen: Conceptualization, Investigation, Methodology, Software, Validation, Visualization, Writing – original draft. **Xiaozhou Xia:** Funding acquisition, Supervision, Writing – review & editing. **Dake Yi:** Funding acquisition, Project administration, Supervision, Writing – review & editing. **Zhongmin Xiao:** Writing – review & editing.

Acknowledgment

This work was supported by the National Natural Science Foundation of China (Grant Nos. 11932006, 12202314, 12172121, and 12002118).

References

[1] Y.-L. Lee, M.E. Barkey, H.-T. Kang, Metal Fatigue Analysis Handbook: Practical Problem-Solving Techniques for Computer-Aided Engineering, Elsevier/BH, Butterworth Heinemann: Amsterdam, 2012.
[2] Z.S. Hosseini, M. Dadfarnia, B.P. Somerday, P. Sofronis, R.O. Ritchie, On the theoretical modeling of fatigue crack growth, J. Mech. Phys. Solids. 121 (2018) 341–362, doi:10.1016/j.jmps.2018.07.026.
[3] P. Paris, F. Erdogan, A Critical analysis of crack propagation laws, J. Basic Eng. 85 (4) (1963) 528–533, doi:10.1115/1.3656900.
[4] M.B. Cortie, G.G. Garrett, On the correlation between the c and m in the paris equation for fatigue crack propagation, Eng. Fract. Mech. 30 (1) (1988) 49–58, doi:10.1016/0013-7944(88)90254-8.
[5] K. Walker, The Effect of Stress Ratio During Crack Propagation and Fatigue for 2024-T3 and 7075-T6 Aluminum, in: M Rosenfeld (Ed.), Effects of Environment and Complex Load History on Fatigue Life, ASTM International: 100 Barr Harbor Drive, PO Box C700, West Conshohocken, PA 19428-2959, 1970 pp 1-1–14, doi:10.1520/STP32032S.
[6] R.G. Forman, V.E. Kearney, R.M. Engle, Numerical analysis of crack propagation in cyclic-loaded structures, J. Basic Eng. 89 (3) (1967) 459–463, doi:10.1115/1.3609637.
[7] M. Shariati, E. Mohammadi, R. Masoudi Nejad, Effect of a new specimen size on fatigue crack growth behavior in thick-walled pressure vessels, Int. J. Pressure Vessels Piping 150 (2017) 1–10, doi:10.1016/j.ijpvp.2016.12.009.
[8] K.L. Roe, T. Siegmund, An Irreversible Cohesive Zone Model for Interface Fatigue Crack Growth Simulation, Eng. Fract. Mech. 70 (2) (2003) 209–232, doi:10.1016/S0013-7944(02)00034-6.
[9] Q. Zhang, Z. Xu, W. Tao, Rate dependent cohesive zone model for fatigue crack growth, Int. J. Mech. Sci. (2024) 109144, doi:10.1016/j.ijmecsci.2024.109144.
[10] A. Ziccarelli, A. Kanvinde, G. Deierlein, Cyclic adaptive cohesive zone model to simulate ductile crack propagation in steel structures due to ultra-low-cycle fatigue, Fatigue Fract. Eng. Mat. Struct. 46 (5) (2023) 1821–1836, doi:10.1111/ffe.13964.
[11] D.S. Dugdale, Yielding of Steel Sheets Containing Slits, J. Mech. Phys. Solids. 8 (2) (1960) 100–104, doi:10.1016/0022-5096(60)90013-2.
[12] M. Kuna, S. Roth, General Remarks on Cyclic Cohesive Zone Models, Int. J. Fract. 196 (1–2) (2015) 147–167, doi:10.1007/s10704-015-0053-y.
[13] O. Nguyen, E.A. Repetto, M. Ortiz, R.A. Radovitzky, A Cohesive Model of Fatigue Crack Growth, Int. J. Fract. 110 (4) (2001) 351–369, doi:10.1023/A:1010839522926.
[14] S. Maiti, P.H. Geubelle, A Cohesive Model for Fatigue Failure of Polymers, Eng. Fract. Mech. 72 (5) (2005) 691–708, doi:10.1016/j.engfracmech.2004.06.005.
[15] Z.-H. Song, N.-Z. Chen, A Modified Cyclic Cohesive Zone Model for Low-Cycle Fatigue Crack Initiation Prediction for Subsea Pipelines under Mode I Loading, Ocean Engineering 276 (2023) 114200, doi:10.1016/j.oceaneng.2023.114200.
[16] T. Zheng, N.-Z. Chen, A Cyclic Cohesive Zone Model for Predicting Hydrogen Assisted Fatigue Crack Growth (FCG) of Subsea Pipeline Steels, Int. J. Fatigue 173 (2023) 107707, doi:10.1016/j.ijfatigue.2023.107707.
[17] Y. Wu, A. Xing, Q. Cheng, Q. Li, Interface Strength Investigations of 304 Stainless Steel/T2 Red Copper T-Type Brazed Joint Based on Cohesive Zone Model, Mater. Res. Express 10 (1) (2023) 016517, doi:10.1088/2053-1591/acb252.
[18] C. Sonsino, Course of SN-Curves Especially in the High-Cycle Fatigue Regime with Regard to Component Design and Safety, Int. J. Fatigue 29 (12) (2007) 2246–2258, doi:10.1016/j.ijfatigue.2006.11.015.
[19] D.A. Jones, High- and Low-frequency Fatigue Revisited, Acta Physiol. Scand. 156 (3) (1996) 265–270, doi:10.1046/j.1365-201X.1996.192000.x.
[20] S. Farfan, High Cycle Fatigue, Low-cycle Fatigue and Failure Modes of a Carburized Steel, Int. J. Fatigue 26 (6) (2004) 673–678, doi:10.1016/j.ijfatigue.2003.08.022.
[21] R. Douglas, W. Beard, N. Barnard, S. Lee, S. Shao, N. Shamsaei, T. Jones, R. Lancaster, The Influence of Energy Density on the Low Cycle Fatigue Behaviour of Laser Powder Bed Fused Stainless Steel 316L, Int. J. Fatigue 181 (2024) 108123, doi:10.1016/j.ijfatigue.2023.108123.
[22] C. Wu, Y. Liu, S. Hu, Y. Lu, C. Guo, H. Li, H. Qu, X. Fu, H. Li, Correlation between Microstructural Evolution and Mechanical Properties of CMDB Propellant during Uniaxial Tension, Propellants Explo Pyrotec 48 (10) (2023) e202300117, doi:10.1002/prep.202300117.
[23] S. Jain, S.R. Na, K.M. Liechti, R.T. Bonnecaze, Characteristic Scaling Equations for Softening Interactions between Beams, Int. J. Fract. 201 (1) (2016) 1–9, doi:10.1007/s10704-016-0106-x.
[24] R. Giusti, G. Lucchetta, Cohesive Zone Modeling of the Interface Fracture in Full-Thermoplastic Hybrid Composites for Lightweight Application, Polymers. (Basel) 15 (22) (2023) 4459, doi:10.3390/polym15224459.
[25] H. Zhang, Y. Huang, S. Xu, S. Natarajan, F. Yao, An Explicit Methodology of Random Fibre Modelling for FRC Fracture Using Non-Conforming Meshes and Cohesive Interface Elements, Compos. Struct. 310 (2023) 116762, doi:10.1016/j.compstruct.2023.116762.
[26] C.G. Dávila, M.W.A Joosten, Cohesive Fatigue Model for Composite Delamination Based on a New Material Characterization Procedure for the Paris Law, Eng. Fract. Mech. 284 (2023) 109232, doi:10.1016/j.engfracmech.2023.109232.
[27] S. Mukhopadhyay, S. Bhatia, Accurate Coarse Mesh Simulation of Delamination in Composites Using a Novel Hp -Adaptive Cohesive Element, J. Compos. Mater. 57 (13) (2023) 2201–2218, doi:10.1177/00219983231169677.
[28] H. Yu, Y.-L. Bai, J.-G. Dai, W.-Y. Gao, Finite Element Modeling for Debonding of FRP-to-Concrete Interfaces Subjected to Mixed-Mode Loading, Polymers. (Basel) 9 (12) (2017) 438, doi:10.3390/polym9090438.
[29] G. Li, C. Li, Linking Bilinear Traction Law Parameters to Cohesive Zone Length for Laminated Composites and Bonded Joints, Advances in aircraft and spacecraft science 1 (2) (2014) 177–196, doi:10.12989/AAS.2014.1.2.177.
[30] W. Jiang, S.R. Hallett, B.G. Green, M.R. Wisnom, A Concise Interface Constitutive Law for Analysis of Delamination and Splitting in Composite Materials and Its Application to Scaled Notched Tensile Specimens, Numerical Meth Engineering 69 (9) (2007) 1982–1995, doi:10.1002/nme.1842.
[31] K. Rege, H.G. Lemu, A Review of Fatigue Crack Propagation Modelling Techniques Using FEM and XFEM, IOP Conf. Ser.: Mater. Sci. Eng. 276 (2017) 012027, doi:10.1088/1757-899X/276/1/012027.